Supporting infromation

Rapid and Precise Tumor Cell Separation Using the Combination of Size-Dependent Inertial and Size-Independent Magnetic Methods

Di Huang[1,2], Nan Xiang[2]*

[1]School of Mechatronic Engineering, China University of Mining and Technology, Xuzhou 221116, P.R. China

[2]School of Mechanical Engineering, Jiangsu Key Laboratory for Design and Manufacture of Micro-Nano Biomedical Instruments, Southeast University, Nanjing 211189, P. R. China

*E-mail: nan.xiang@seu.edu.cn; Tel: +86 (025) 52090508; Fax: +86 (025) 52090501.

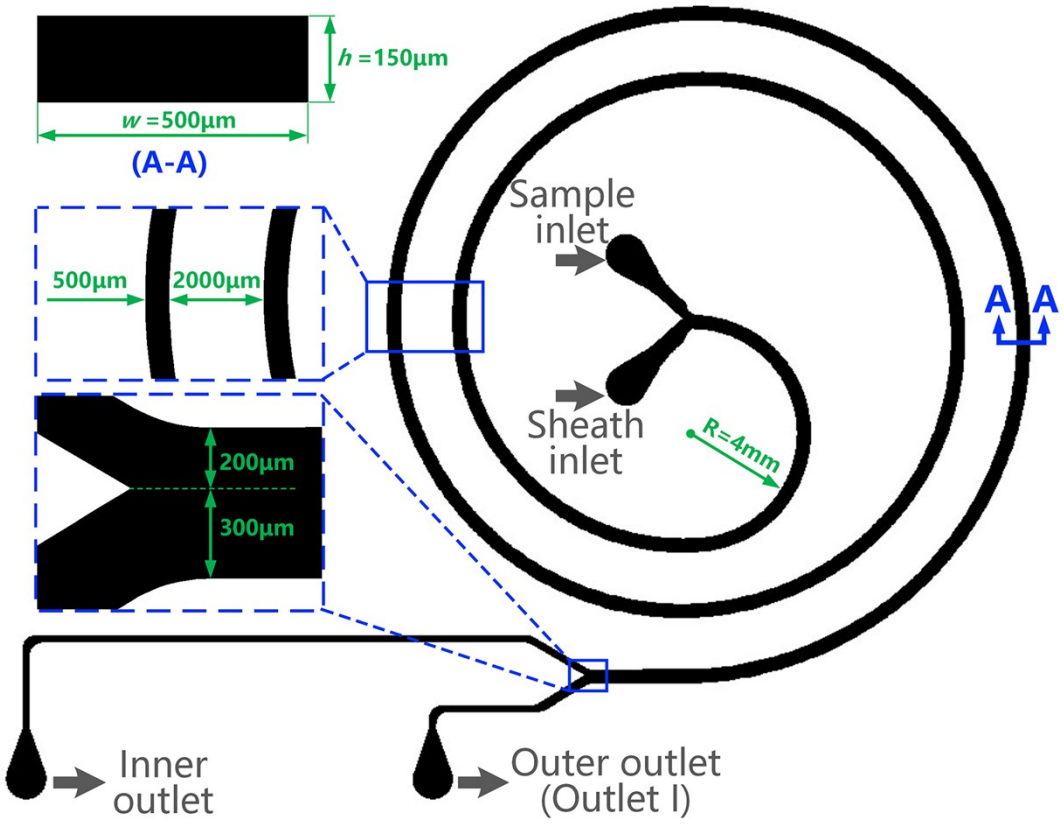

Figure S1. Structure of the first-stage spiral inertial sorter. The spiral inertial sorter consists of a 2-loop Archimedean spiral microchannel with two inlets and two outlets. The spiral microchannel has a low aspect ratio (h/w = 0.3) cross-section of 150 μm in height and 500 μm in width. The radius of the innermost channel loop is 4 mm, and the distance between two adjacent loops is 2000 μm. In the end of the spiral channel, a bifurcated outlet system (inner outlet: outer outlet = 2:3) was applied to remove the separated RBCs or to export the tumor cells and WBCs into the second-stage focuser.

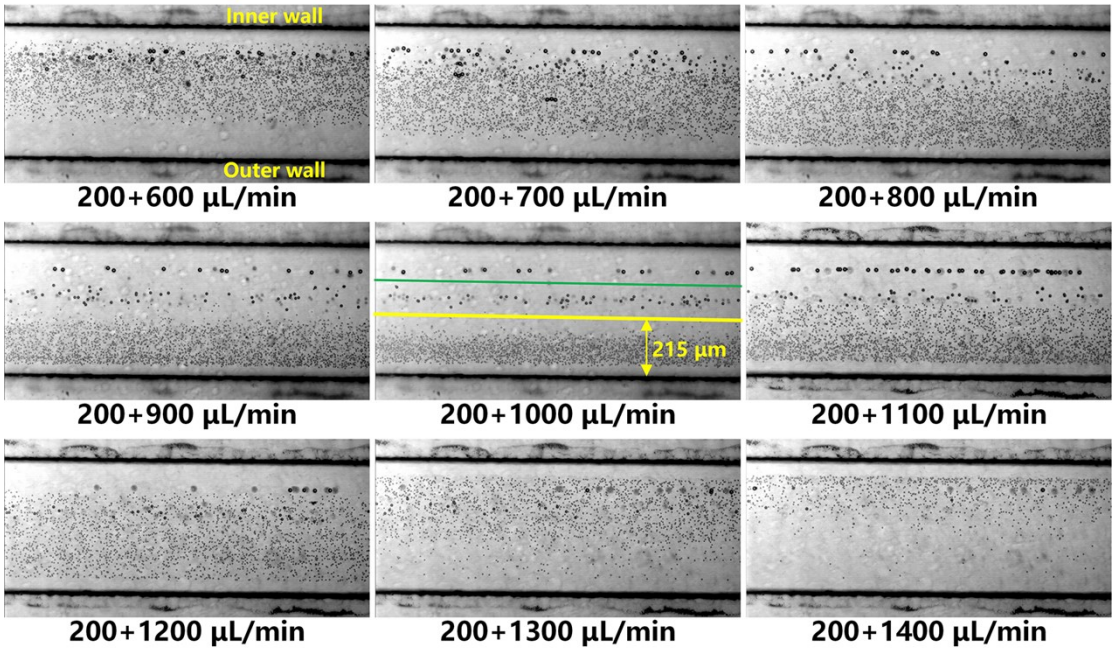

Figure S2. The distributions of 4.8 µm, 10 µm and 15 µm particles across the channel width near the outlet of the spiral inertial sorter at the total flow rates of 800~1600 µL/min. The sample flow rate was fixed at 200 µL/min while the sheath flow rate increased from 600 µL/min to 1400 µL/min. The result indicated that the best separation performance was observed at the sheath flow rate of 1000 µL/min. At this optimal flow rate, the small 4.8 µm particles flowed along Dean vortex and travelled to a narrow region close to the outer wall (less than 215 µm), while the large 15 µm particles were focused near the inner wall and the 10 µm particles were focused near the channel centerline.

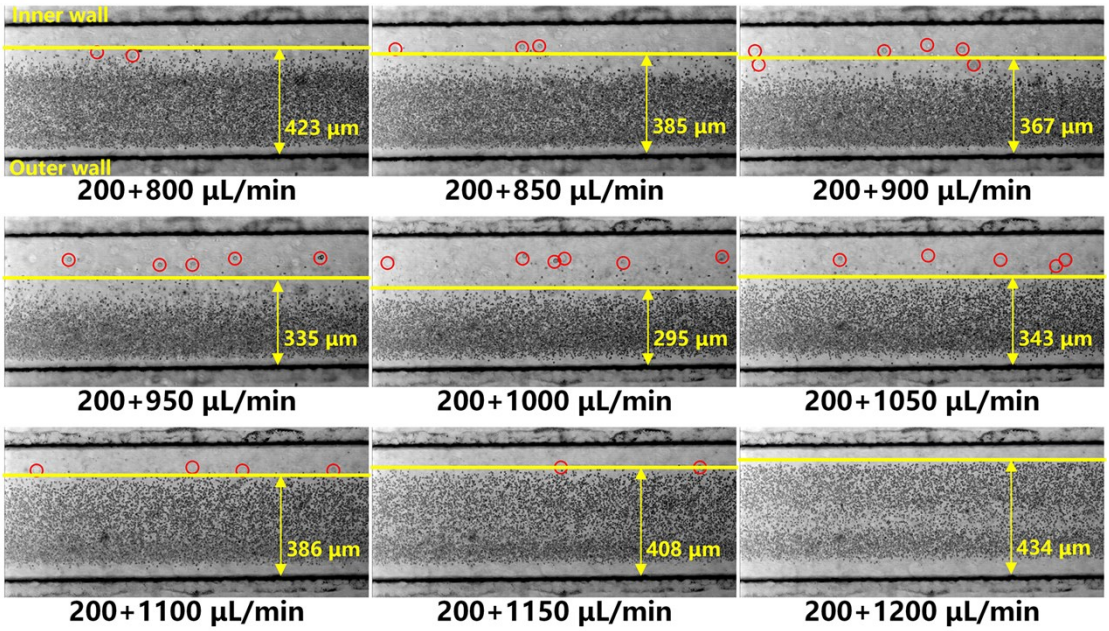

Figure S3. The distributions of tumor cells and blood cells across the channel width near the outlet of the spiral inertial sorter at the total flow rates of 1000~1400 μL/min. The sample flow rate was fixed at 200 μL/min and the sheath flow rate increased from 600 μL/min to 1400 μL/min. The concentrations of tumor cells and blood cells for the current experiments were controlled to be 10^5 counts/mL and 10^8 counts/mL, respectively. The larger tumor cells were marked by red circles. The result indicated that the smaller RBCs stream have the narrowest width of 295 μm near the outer wall at the sheath flow rate of 1000 μL/min, which was consistent with particle experiment described in Figure S2 and verified the reliability of the optimal flow rate (200+1000 μL/min). According to the current experimental results, the width of inner and outer outlets of spiral inertial sorter could also be determined as 200 μm and 300 μm, respectively.

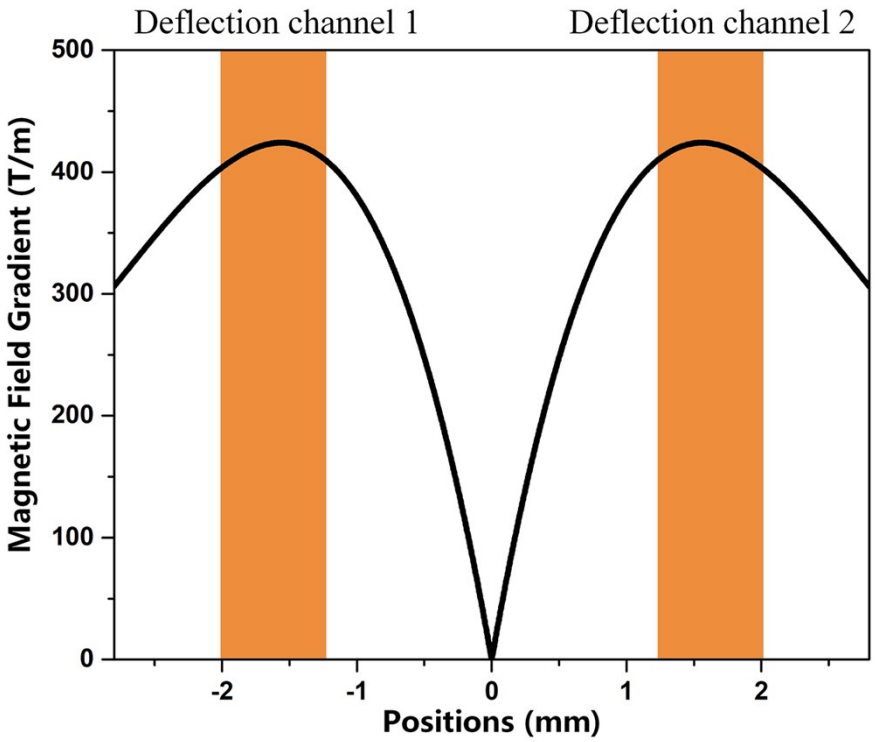

Figure S4. Calculation result of the magnetic field gradient based on ANSYS Maxwell 2D model. The two magnetic deflection channels were placed at the strongest magnetic field gradient area.

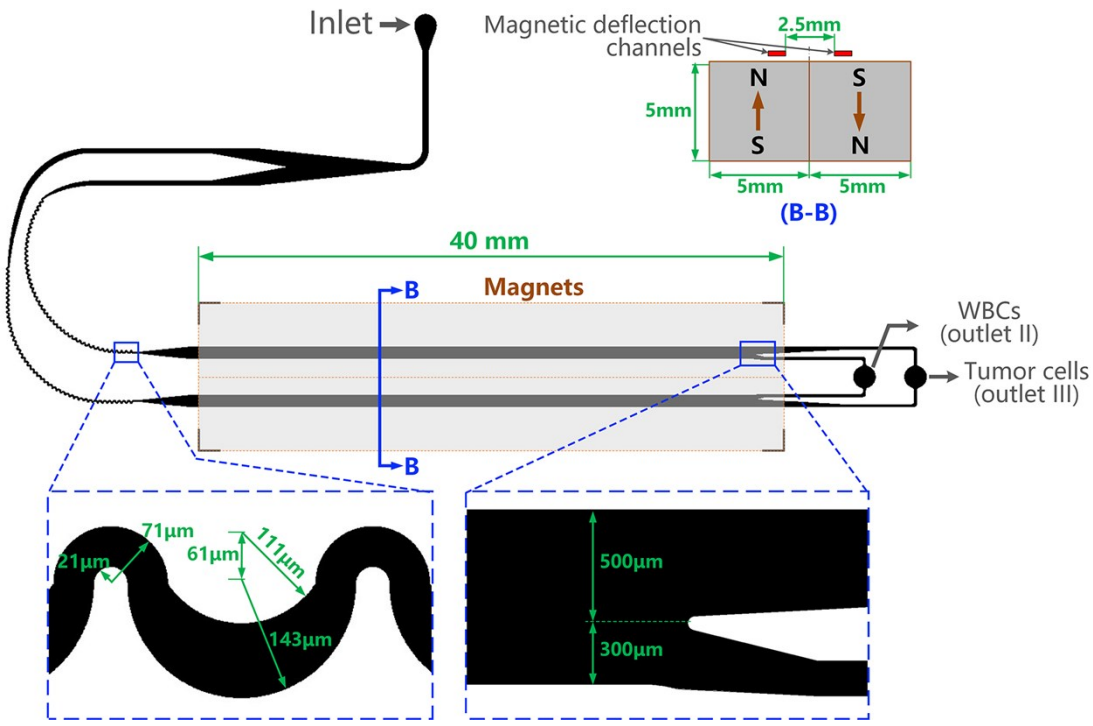

Figure S5. Structure of the second-stage serpentine focuser and the third-stage magnetic sorter. The inlet was connected to the inner outlet of spiral inertial sorter and then bifurcated into two branches with the same function to increase throughput. Each branch was composed of a serpentine channel and a directly connected magnetic deflection channel. The serpentine channel was arranged along a curve shape to reduce the device footprint. Each repeated unit of the serpentine channel consists of a large curving turn with a radius of 111 μm and a small curving turn with a radius of 21 μm. The width of the small turn was designed to be 50 μm, while the large turn smoothly connects with the small turn and has variable widths. Each of the straight magnetic deflection channel has a length of 40 mm and a width of 800 μm. The distance between the two magnetic deflection channels was determined to be 2.5 mm according to the calculated magnetic field gradient. At the rear end of the magnetic deflection channels, bifurcated outlet systems (outer part: inner part =5:3) were applied to export the target tumor cells or to remove the separated labeled WBCs, and the corresponding outlets were connected together to simplify the operation. The height of the serpentine channel and the magnetic deflection channel are 60 μm.

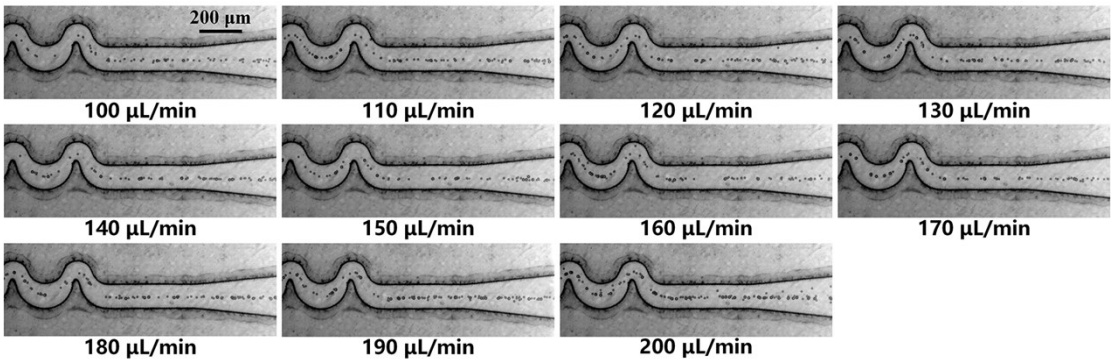

Figure S6. The distributions of 10 μm and 15 μm particles across the channel width at the rear end of serpentine channels at the flow rates of 100~200 μL/min. The flow rates in this figure are the total flow rates from the inlet that marked in Figure S4 (the same below).

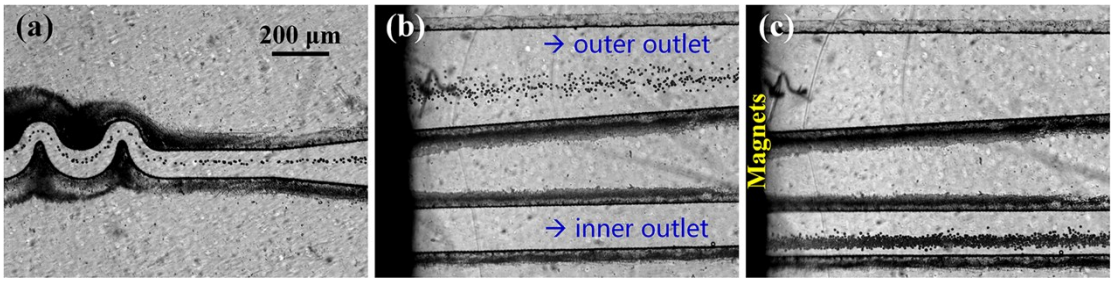

Figure S7. (a) 10 µm magnetic particles focused in a single line through the serpentine channel. (b) 10 µm magnetic particles directly entered the outer outlet without magnetic field. (c) 10 µm magnetic particles deflected into the inner outlet when the magnetic field was applied.

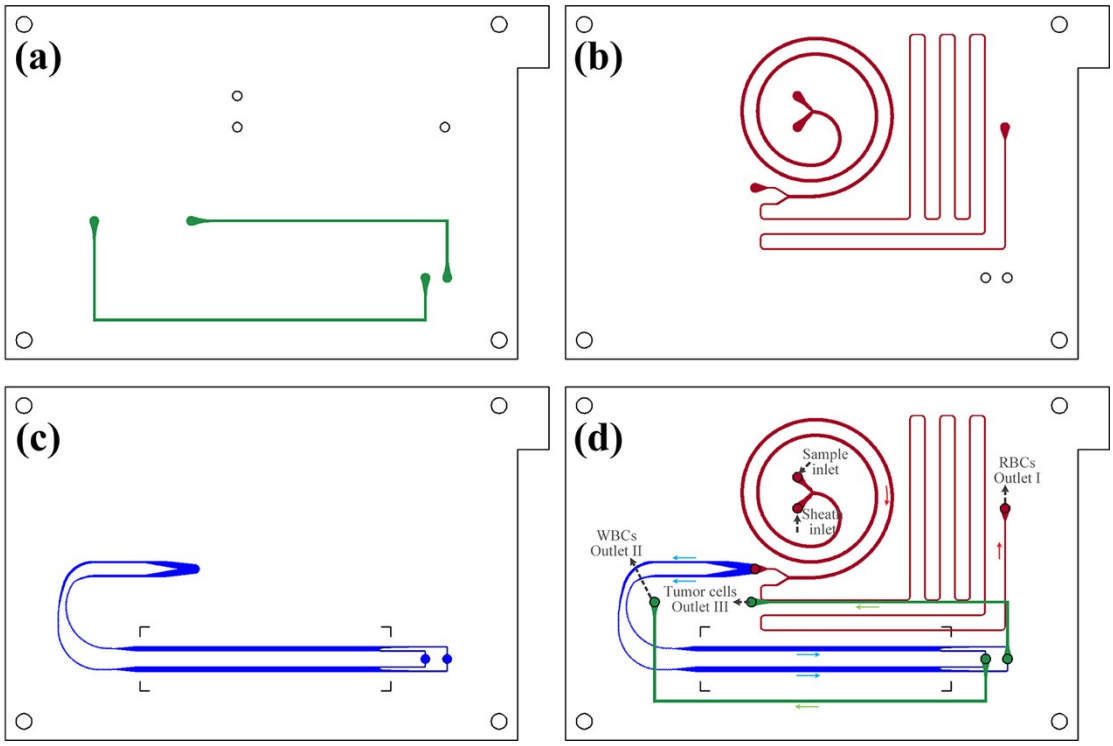

Figure S8. CAD drawing illustrating the detailed structures of (a) outlet chip, (b) spiral inertial sorter chip, and (c) serpentine focuser & Magnetic sorter chip. (b) CAD drawing of our vertically stacked i-Mag device. The solid arrows with different colors indicate the flow directions in different layers.

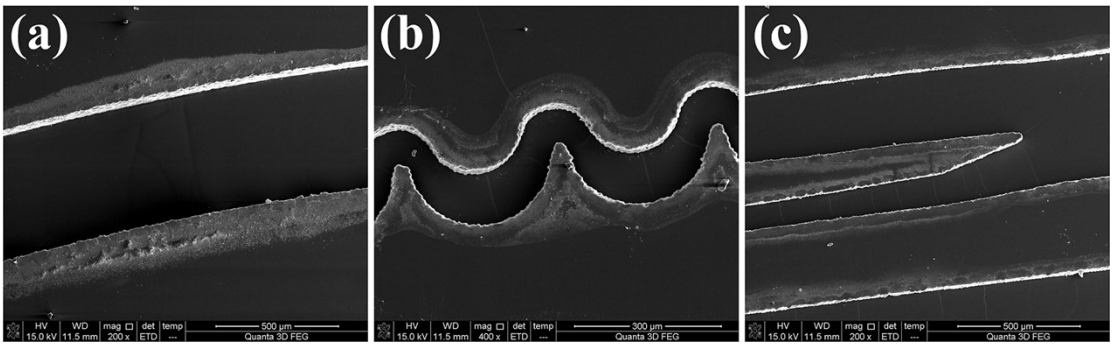

Figure S9. SEM images of the fabricated (a) spiral channel, (b) serpentine channel and (c) magnetic deflection channel.

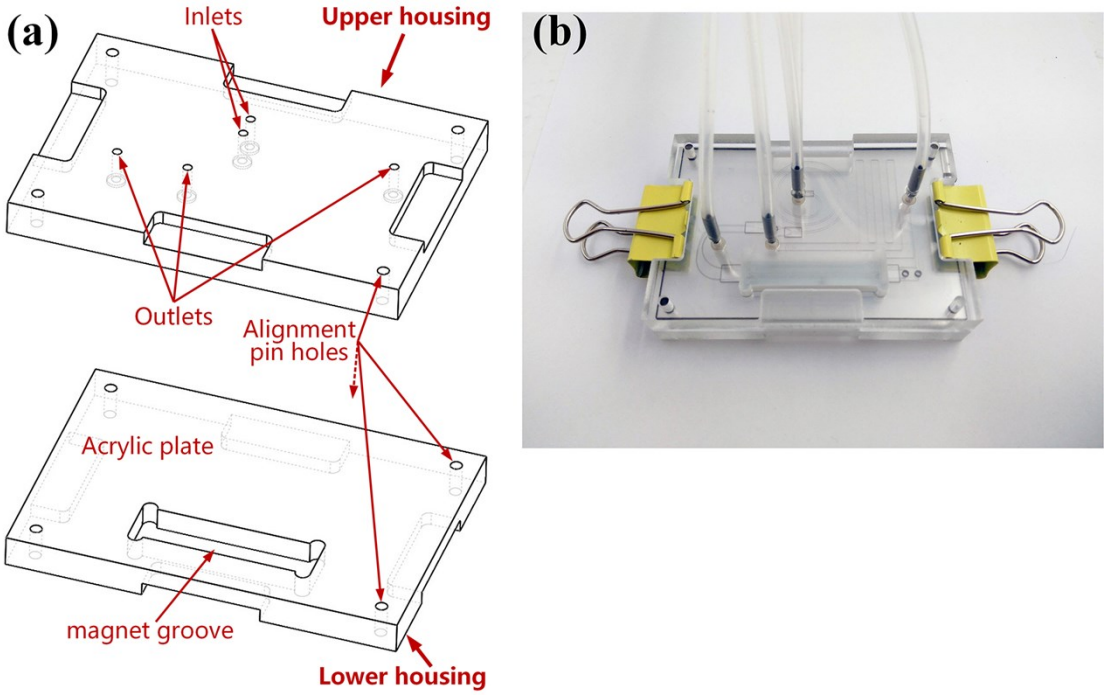

Figure S10. (a) Schematic diagram illustrating the structure of the housing. (b) Photograph of the custom housing equipped with our i-Mag device.

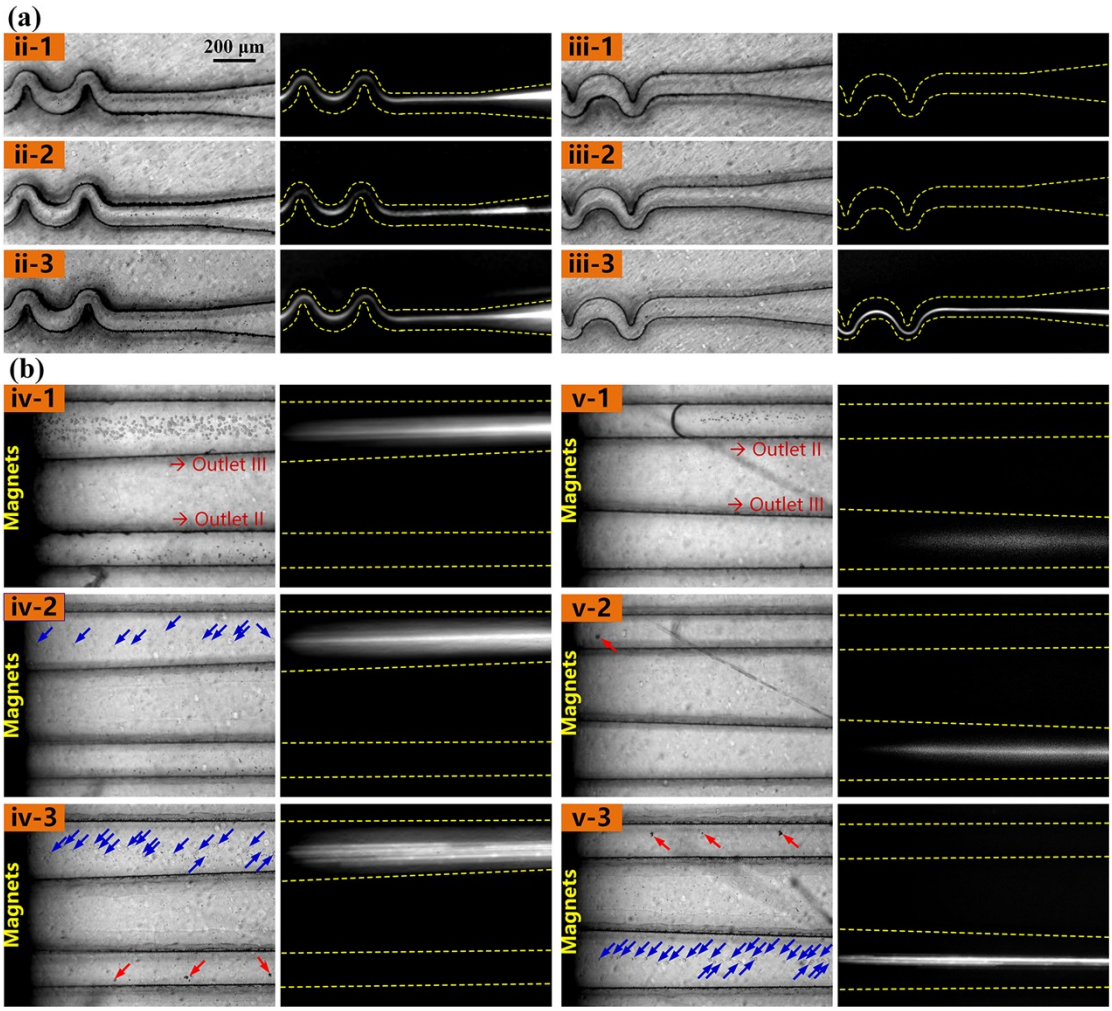

Figure S11. Cell distributions in (a) serpentine focuser and (b) magnetic sorter. The suffix numbers after each location indicate different layers. In these images, the beads-labeled WBCs were marked with red arrows, while the blue arrows indicated tumor cells.

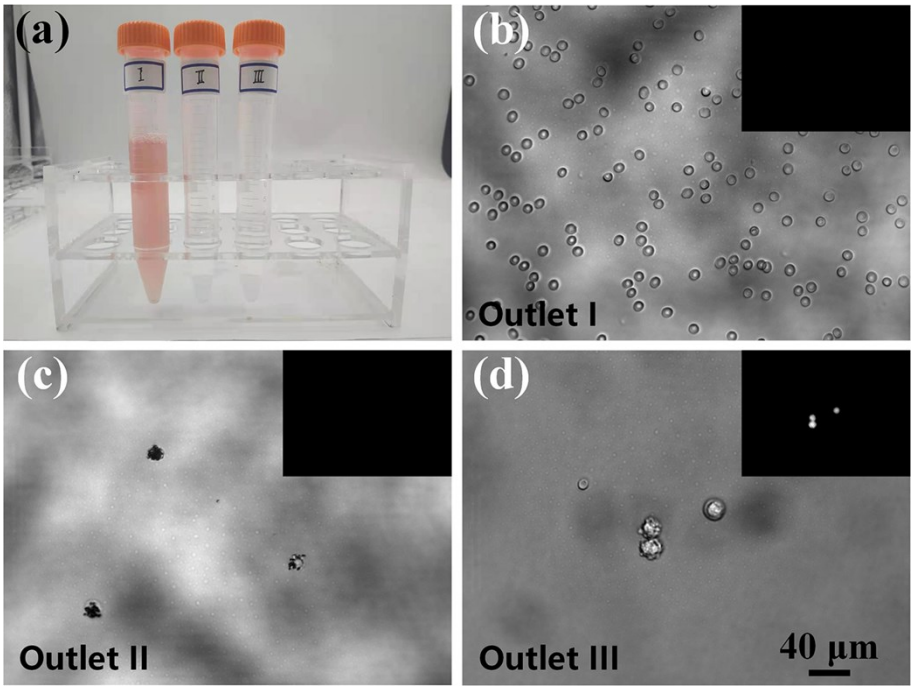

Figure S12. (a) Photograph of the collected samples from the experiment of separating human lung cancer cells A549 from blood, and microscopic images of samples collected from (b) outlet I, (c) outlet II, and (d) outlet III. The fluorescence images in the upper right corners were used to identify the stained tumor cells.

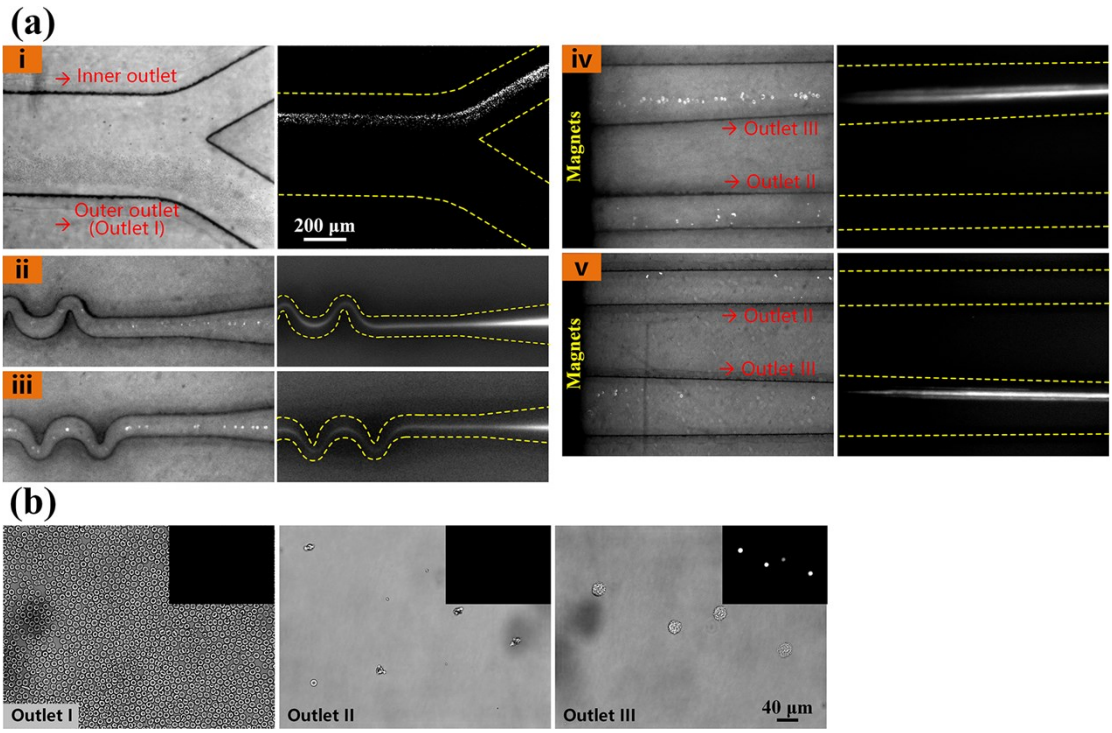

Figure S13. (a) Composite images acquired from both bright-field mode and fluorescence mode illustrating the particles distributions at representative locations. (b) Microscopic images of the samples collected from three outlets.

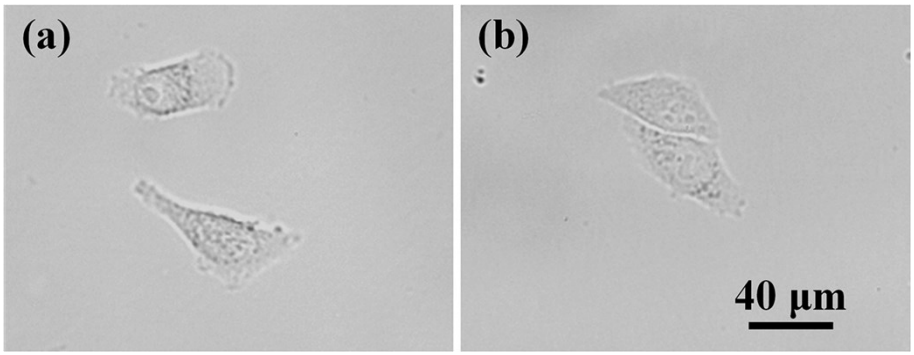

Figure S14. Microscopic images of the separated tumor cells which were re-cultured for (a) 24 hours and (b) 48 hours.

Table S1. A comparison of the device performances between different combinatorial methods

Method	Application	Performance	Ref.
DLD + Magtrophoresis	Tumor antigen-independent sorting of tumor cell lines from blood	Captured efficiency: ~96.7%; Purification: 2.5 log (mean, 32,000 WBCs/ml)	Ozkumur, et, al.[1]
DLD + Magtrophoresis	High-throughput blood cell depletion to sort tumor cell lines	Throughput: debulking of blood samples at 15-20 million cells per second; Recovery: 99.5%; WBC carryover of 445/mL	Fachin, et,al.[2]
Eluting on a modified Gilson PIPETMAX	Isolation of rare breast and prostate cancer cells from PBMCs	Purity: an average of only 95 contaminant cells captured per milliliter of processed whole blood. Capture efficacy: ranging from ~40% (HCCs) to >95% (LNCaPs).	Pezzi, et,al.[3]
Ferrohydrodynamic cell separation	Enrichment of several cancer cell lines from blood	Throughput: 200 μL/min; Recovery rate: 99.08% at down to ∼10 cells per mL spike ratio; Purity: low WBC contamination (533 cells for every one milliliter blood processed)	Zhao, et, al.[4]
Double spiral + integrated filter	Isolation and mRNA detection of lung adenocarcinoma cells A549	Capture efficiency: 74.4%	Wang, et,al.[5]
MOFF+DEP	Separation of MCF-7 cells from diluted blood	Enrichment factor: 162 Throughput: 126 μL/min RBCs depletion: 99.24% WBCs depletion: 94.23%	Moon, et,al.[6]
Spiral + magnetophoresis	Separation of human breast and lung cancer cells from blood	Separation efficiency: 93.84% Purity: 4.39-51.47% Blood cell remove ratio: >99.83% Throughput: 200 μL/min	This article

1. E. Ozkumur, A. M. Shah, J. C. Ciciliano, B. L. Emmink, D. T. Miyamoto, E. Brachtel, M. Yu, P. I. Chen, B. Morgan, J. Trautwein, A. Kimura, S. Sengupta, S. L. Stott, N. M. Karabacak, T. A. Barber, J. R. Walsh, K. Smith, P. S. Spuhler, J. P. Sullivan, R. J. Lee, D. T. Ting, X. Luo, A. T. Shaw, A. Bardia, L. V. Sequist, D. N. Louis, S. Maheswaran, R. Kapur, D. A. Haber and M. Toner, *Sci. Transl. Med.*, 2013, **5**, 179ra147.
2. F. Fachin, P. Spuhler, J. M. Martel-Foley, J. F. Edd, T. A. Barber, J. Walsh, M. Karabacak, V. Pai, M. Yu, K. Smith, H. Hwang, J. Yang, S. Shah, R. Yarmush, L. V. Sequist, S. L. Stott, S. Maheswaran, D. A. Haber, R. Kapur and M. Toner, *Sci. Rep.*, 2017, **7**, 1-11.
3. H. M. Pezzi, D. J. Guckenberger, J. L. Schehr, J. Rothbauer, C. Stahlfeld, A.

Singh, S. Horn, Z. D. Schultz, R. M. Bade, J. M. Sperger, S. M. Berry, J. M. Lang and D. J. Beebe, *Lab Chip*, 2018, **18**, 3446-3458.

4. W. J. Zhao, Y. Liu, B. D. Jenkins, R. Cheng, B. N. Harris, W. Z. Zhang, J. Xie, J. R. Murrow, J. Hodgson, M. Egan, A. Bankey, P. G. Nikolinakos, H. Y. Ali, K. Meichner, L. A. Newman, M. B. Davis and L. D. Mao, *Lab Chip*, 2019, **19**, 1860-1876.
5. J. D. Wang, W. J. Lu, C. H. Tang, Y. Liu, J. S. Sun, X. Mu, L. Zhang, B. Dai, X. Y. Li, H. L. Zhuo and X. Y. Jiang, *Anal. Chem.*, 2015, **87**, 11893-11900.
6. H. S. Moon, K. Kwon, S. I. Kim, H. Han, J. Sohn, S. Lee and H. I. Jung, *Lab Chip*, 2011, **11**, 1118-1125.